Research Article | Vol. 12, No. 1 / 1 January 2021 / Biomedical Optics Express 588
Biomedical Optics EXPRESS

Quantitative measurement of mechanical properties in wound healing processes in a corneal stroma model by using vibrational optical coherence elastography (OCE)

YILONG ZHANG,[1] YUTING LING,[1] DUO ZHANG,[1] MINGKAI WANG,[1] CHRISTINE PURSLOW,[2] YING YANG,[3] CHUNHUI LI,[1] AND ZHIHONG HUANG[1,*]

[1]School of Science and Engineering, University of Dundee, Dundee DD1 4HN, Scotland, UK
[2]Thea Pharmaceuticals Ltd, Keele University Science & Innovation Park, Innovation Way, Stoke-on-Trent, ST5 5NT, UK
[3]Guy Hilton Research Center, School of Pharmacy and Bioengineering, Keele University, Stoke-on-Trent, ST4 7QB, UK
[*]z.y.huang@dundee.ac.uk

Abstract: Corneal wound healing, caused by frequent traumatic injury to the cornea and increasing numbers of refractive surgeries, has become a vital clinical problem. In the cornea, wound healing is an extremely complicated process. However, little is known about how the biomechanical changes in wound healing response of the cornea. Collagen-based hydrogels incorporating corneal cells are suitable for replicating a three-dimensional (3D) equivalent of the cornea *in-vitro*. In this study, the mechanical properties of corneal stroma models were quantitatively monitored by a vibrational optical coherence elastography (OCE) system during continuous culture periods. Specifically, human corneal keratocytes were seeded at 5×10^5 cells/mL in the hydrogels with a collagen concentration of 3.0 mg/mL. The elastic modulus of the unwounded constructs increased from 2.950 ± 0.2 kPa to 11.0 ± 1.4 kPa, and the maximum thickness decreased from 1.034 ± 0.1 mm to 0.464 ± 0.09 mm during a 15-day culture period. Furthermore, a traumatic wound in the construct was introduced with a size of 500 μm. The elastic modulus of the neo-tissue in the wound area increased from 1.488 ± 0.4 kPa to 6.639 ± 0.3 kPa over 13 days. This study demonstrates that the vibrational OCE system is capable of quantitative monitoring the changes in mechanical properties of a corneal stroma wound model during continuous culture periods and improves our understanding on corneal wound healing processes.

1. Introduction

The cornea, as the outmost surface of the anterior eye, is responsible for approximately 2/3 of the total refractive power to focus light onto the retina for vision [1] and it also acts as the major barrier for the eye from infectious agents [2]. Corneal wound healing, caused by frequent traumatic injury to the cornea and increasing numbers of refractive surgeries, become a vital clinical problem [3]. When chemical or physical injuries occur on the cornea, scarring will form [4]. Untreated eye injuries or improper treatment can lead to disrupted vision and increasing risk of bacterial infections, causing severe damage to the cornea and even permanent vision loss [5]. However, current clinical treatments for corneal injuries, are usually through topical antibiotics to minimise pain and infection, rather than focusing on the wound healing process, which may have no effect on or delay wound healing [6]. Therefore, corneal wound healing is not only an important clinical issue, but there is also a need to better understand the chemical and physical mechanism of cellular behaviour, in order to improve and accelerate the healing process.

#404096 https://doi.org/10.1364/BOE.404096
Journal © 2021 Received 30 Jul 2020; revised 16 Nov 2020; accepted 17 Nov 2020; published 22 Dec 2020

Biomedical Optics EXPRESS

Corneal wound healing is an extremely complicated process, including the simultaneous multiple biochemical signals to regulate activities of cells alongside the chemical and biophysical characters of cellular matrix in the wound area [3,7]. Indeed, studies have investigated the soluble signalling factors acting on the corneal wound healing, for example, transforming growth factor-β (TGF-β) [8,9]. However, less is known about any internal biomechanical variations during corneal wound healing.

The stroma is an important layer in the cornea, contributing about 80% - 85% of the thickness of the entire cornea. When a corneal injury occurs, the stroma plays a main responsive role to the injury [10]. Keratocytes, also known as stromal fibroblasts, are the primary cell type in the stroma. These cells are capable of synthetizing collagen molecules and glycosaminoglycans to maintain homeostasis in the stroma [2].

To date, tissue engineering has become a promising technique in regenerative medicine through fabricating implants with specialized physical function. In theory, this approach induces differentiation of stem cells, thereby it can realize features of related tissues *in-vitro* [11]. Tissue engineering technique provide a useful *in-vitro* tissue model to replicate physiological mechanism and cell behaviour *in-vivo*. It also has potential in regenerative medicine and reduces the use of animals [12]. Three-dimensional (3D) culture environment reconstruction is one of strengths in tissue engineering, ensuring homeostasis and metabolism of the intrinsic molecules, with highly complexity and multicellular circumstance in a 3D structure [13].

Hydrogel is a popular material in tissue engineering to construct 3D environments due to its viscoelasticity, biocompatibility and ability to transmit nutrients and gases [14]. In many connective tissues, especially the corneal stroma, collagen plays a role as the main mechanical and structural protein in the extracellular matrix (ECM), where collagen type I is the most abundant. Thus, collagen based hydrogels seeded with keratocytes are suitable for modelling the human corneal stroma *in-vitro* [15,16].

The elastic modulus (Young's modulus, E) offers a vital parameter to access the stiffness of materials. Tensile test [17] and compression test [18] are the most common methods to characterise the elasticity of tissue, and also hydrogel. In these two techniques, a stress-strain relationship can be obtained from force applied on and displacement of sample, and then Young's modulus can be calculated from the stress-strain curve. Nevertheless, both two methods are destructive to sample. Indentation techniques have been widely applied to test the mechanical properties of soft materials. In 2008, Ahearne et al. [19] designed a spherical indentation method to monitor the biomechanics in corneal stroma hydrogels during a 14-day culture period. The hydrogels were fixed in a holder and deformed by a hydrophobic ball of known size and weight, and then analysis of the deformation on the hydrogels allowed the elastic modulus to be calculated. This method was non-destructive, but only the mechanical changes in the bulky hydrogels were examined. It was unable to display regional changes in mechanical properties at a resolution of microns in a biological process, such as wound healing process.

An advanced imaging modality, optical coherence tomography (OCT) can acquire 2D and 3D structure image with micro-scale resolution. The imaging depth penetrates up to millimetre scale [20]. Compared to other imaging modalities such as magnetic resonance imaging (MRI), computerised tomography (CT) and ultrasound, OCT has higher resolution and larger imaging capacity in uncovering delicate structures. In addition, OCT, as a non-invasive technology, has been used to monitor morphological change from most transparent tissues, for example, retina [21,22] to multitudinous non-transparent tissues, for example, skin [23], cartilage [24] etc. With the increasing attention to corneal wound healing, OCT has been applied to monitor structural changes in the human [25–28] and animal [29–31] cornea after being injured.

Optical coherence elastography (OCE) is based on OCT, with the added capability of providing microstructure and quantitative measurement of mechanical properties. It has become attractive owing to the potential to provide high imaging resolution for characterisation of tissue stiffness

Biomedical Optics EXPRESS

[32]. The ultra-fast OCE techniques based on swept-laser source have been developed to largely reduce the acquisition time to millisecond scale. Singh et al. [33] demonstrated an ultra-fast shear-wave OCE (SW-OCE) with an A-scan rate of ~1.5 MHz and a frame rate of ~7.3 kHz to image the propagation of the elastic wave in an *ex-vivo* porcine cornea. The lateral field of view of the elastic wave was ~4 mm and continuous B-scans were acquired for ~30 ms. Then, Wu et al. [34] used the same A-scan rate and the frame rate to image the wave propagation, but the shear waves were induced by a magnetic force excitation system instead of an air-pulse excitation. The lateral scanning field was over ~7.9 mm for the agar phantoms and an *ex-vivo* porcine liver. Song et al. [35] developed a SW-OCE with the frame rate up to 16 kHz at an A-line rate of ~1.62 MHz, capable to detect frequency of shear waves up to 8 kHz for the *ex-vivo* porcine cornea. The lateral and axial scan range was 3.7 mm and 4 mm, respectively. However, there is an inherent trade-off between the temporal and lateral spatial resolutions for ultra-fast wave-based OCE [33], also the lateral resolution of wave-based OCE methods is much lower than vibrational OCE [36]. At the meantime, in vibrational OCE, fast Fourier transform (FFT) algorithm used to resolve vibration amplitude can eliminate noise and other co-generated vibrational modes, leading to a high signal to noise ratio (SNR) [37]. The basic principle of vibrational OCE is to initially give a periodic vibration in sample and then detect the vibration amplitude. The area with lower vibration amplitude represents a stiffer material. Inversely, soft material has higher vibration amplitude [38].

This study presents the first investigation of utilizing tissue engineering technique to reconstruct 3D corneal stroma models to those found clinically, and quantitatively measure the changes in biomechanical properties of wound healing in the corneal stroma wound models during a continuous culture period by applying our vibrational OCE system.

2. Materials and methods

2.1. Cell culture

Human corneal keratocytes (P10872; Innoprot) up to passage three were cultured in cell culture flasks with Dulbecco's modified eagle medium (DMEM, 1.0 g/L glucose, no L-Glutamine; Lonza) supplemented with 10% Foetal Bovine Serum (FBS; Gibco), 1% antibiotic and antimitotic solution (PEN-STREP 5000 U Penicillin/m, 5000U Streptomycin/mL; Lonza) and 1% L-glutamine (2 mM; Lonza) in the incubator with 5% carbon dioxide (CO_2) at 37°C.

2.2. Hydrogel preparation

Collagen hydrogels for our study were constructed with DMEM, NaOH and rat-tail collagen type I (3.5 mg/mL, CORNING, USA), according to a previous protocol [39]. To achieve a collagen concentration of 3.0 mg/mL in the volume of 80μL per hydrogel, keratocytes with density of 5×10^5 cells/mL were suspended in DMEM medium, and then mixed evenly with the other components. Hydrogels without cells were also manufactured as a control. In the controls, the volume of cell suspension was substituted with the equal volume of DMEM medium.

As illustrated in Fig. 1, the collagen mixture solution was pipetted onto a number of filter paper rings with an 8-mm outer diameter and 6-mm inner diameter on a hydrophobic polytetrafluoroethylene (PTFE) board piece. The filter paper rings were used to prevent the horizontal contraction of the hydrogels and mimic shape of the hydrogel to the cornea. The total volume of 80 μL per hydrogel could just cover a filter paper ring. The collagen solution mixture was gelated after approximately two hours under 37°C. In total, 29 cell-seeded models and 24 no-cell models were established in this study. All samples were cultured with the supplemented DMEM medium, under 5% CO_2 and 37°C. An overview of the experimental groups of the unwounded and wounded models are listed in Table 1.

Biomedical Optics EXPRESS

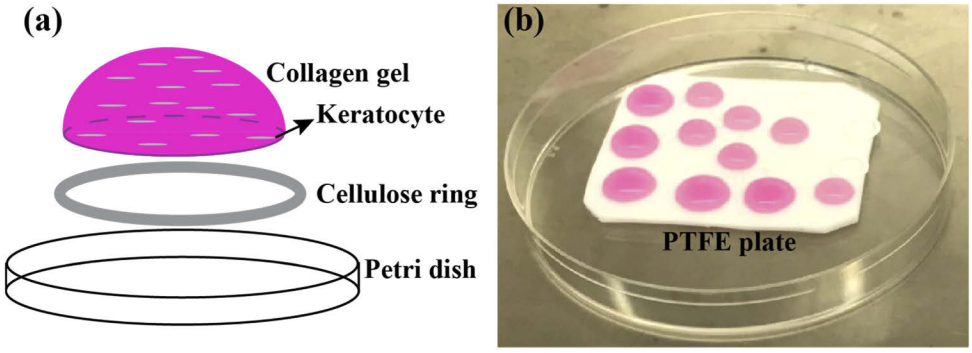

Fig. 1. (a) A sketch of the design of in-vitro 3D corneal stroma models seeded with keratocytes and (b) Collagen hydrogels place on a PTFE board piece in petri dish.

Table 1. An overview of the experimental groups of the unwounded and wounded models

	Unwounded models				Wounded models
	Cell-seeded		No-cell		Cell-seeded
	OCT	OCE	OCT	OCE	OCE
Time points of tests	Day 1, 3, 7, 9, 11, 13, 15				Day 3, 6, 10, 13
Sample number per day	3	3	3	3	5
Total samples	3	21	3	21	5

2.3. Wound in construct

One day after 5 constructs formation in 35-mm petri dishes, a rapid-core sampling tool (WellTech, Taiwan) with needle size of 500 μm was used to introduce a physical wound in the constructs. For each operation, the needle run through the constructs from the central point and was held for 10 s to ensure the repeatability of the wound in each construct.

2.4. Cell morphology

A light microscopy (Olympus CKX41) was constantly employed to view the confluent and morphology of keratocytes in the constructs. The initial 4×10^4 keratocytes seeded in per construct with total volume of 80 μL were constantly recorded over the culture period.

2.5. System setup

A lab-built vibrational OCE based on phase sensitive OCT (PhS-OCT) [40] was applied in this study as the schematic drawing shown in Fig. 2. The vibrational OCE system included a common-path OCE setup as Fig. 2 (tion a) and a dual-arm OCE setup as Fig. 2 (section b). In the common-path OCE, the original reference arm was blocked (Fig. 2 (section c)). A glass imaging window (Ø1" N-BK7 Broadband Precision Window, Uncoated, t = 5 m, Thorlabs) was set at 2 mm below sample window and the lower surface of glass imaging window served as a reference plane to generate optical path difference within a coherence length. In the dual-arm OCE setup, the original reference was used, and the non-contact measurement could be realised. Based on our PhS-OCT system, the SNR of OCE system is 53 dB and the sensitivity of displacement detection is 2 nm. A super luminescent diode (SLD, Thorlabs) with a central wavelength of ~1340 nm and bandwidth of ~110 nm was employed as a light source. The OCT system provides an axial resolution of 7.8 μm in air, corresponding to 5.8 μm in sample (refraction index n=1.343) with an axial sampling distance of 3.8 μm. The penetration depth is up to 2 mm in sample. Meanwhile, the focal length of objective lens is 50 mm and the lateral resolution is 16 μm. Interfering signal

Biomedical Optics EXPRESS

is detected and collected by a high-speed InGaAs line scan camera (SUI, Goodrich Corp, NJ, USA) and a transmission grating (1,200 lines/mm) lens at maximum sampling frequency with 91,912 kHz.

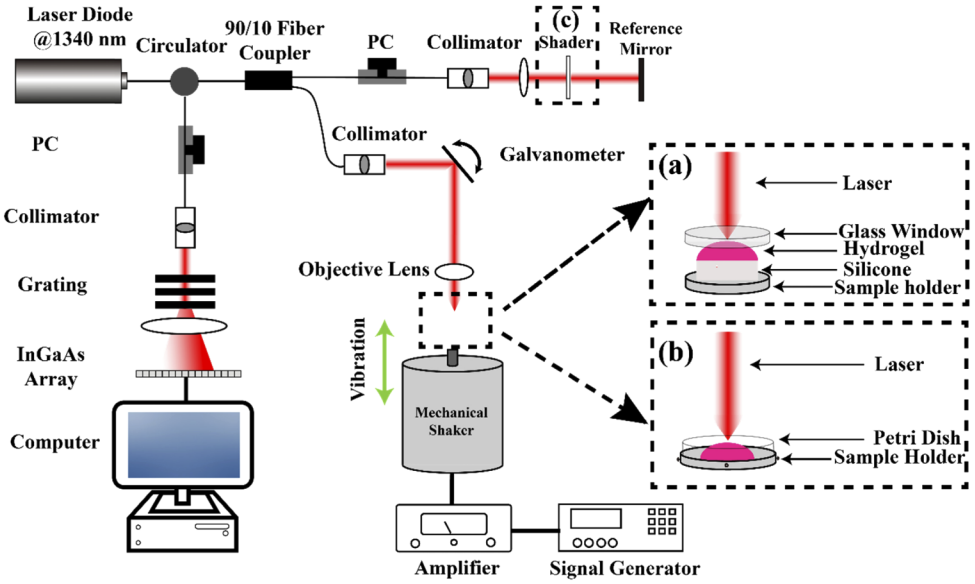

Fig. 2. A schematic of vibrational OCE system consists of a common-path OCE setup (section a) and a dual-arm OCE setup (section b), on the basis of PhS-OCT system. In the common-path OCE, the original reference arm was blocked by a shader (section c) and the lower surface of the imaging glass window served as reference plane. The dual-arm OCE setup used the original reference arm. The mechanical shaker generated sinusoidal vibration, that was parallel to laser light in axial direction. PC: Polarization Controller

In our current vibrational OCE, periodic vibration was provided in vertical axis. A sinusoidal signal with frequency of 225 Hz and amplitude of 20 milli-volts peak-to-peak (mVpp) was generated by a waveform generator (Agilent Technologies, USA). An amplifier (AE Techron) was used to drive a magnet shaker (Brüel & Kjær Sound & Vibration Measurement A/S, Denmark). The displacement in sample was measured to be within 1 μm. Scanning protocol of cross-sectional image used MB-scan, where each M scan consisted of 512 A-scans and 512 M-scan formed one complete B scan. The sampling speed was set as 10,360 A-lines/s.

In order to monitor the change in stiffness of the unwounded models by the common-path OCE (Fig. 2 (section a)), the unwounded constructs and the controls were successively transferred from 48-well plate to a cylindrical silicone (Ecoflex 00–30, Smooth-on Inc, USA) on the magnet shaker. The silicone was fabricated according to the manufacture manual with a height of 1 mm, a diameter of 8 mm and elasticity of ~222 kPa (the detection method and the results were included in Supplemental material). The movement of the shaker was adjustable in axial and lateral directions. Then, the unwounded models were elevated to contact with the glass window and the displacement was measured with a micrometre calliper. The stiffness of the unwounded models was calibrated by the silicone with known stiffness underneath at different time points over the culture period in this step.

To monitor the maximum thickness of the unwounded models and the stiffness change in the wounded constructs during wound healing by the dual-arm OCE (Fig. 2 (section b)), the unwounded models and the wounded constructs in 35-mm petri dishes with culture medium removed was placed in a round-shape sample holder, where the models remained in a sterile

Biomedical Optics EXPRESS

environment with the glass lid on top and was sealed with parafilm to keep hydrated during imaging process. Once OCT and OCE imaging acquisition completed, unwounded models and constructs were returned back to the incubator with culture medium refreshed and repeated this procedure on the next measurement time point. As the surrounding normal tissue in the wounded constructs could be assumed to have an equivalent stiffness to the unwounded constructs at the same time point, the stiffness of the neo-tissue in the wounded constructs was measured via comparing with the surrounding normal tissue in this step.

The acquisition time of 2D OCT image was 0.06 s (1.2 scanning cycle × 512 scanning points /10,360 sampling frequency) and for 2D OCE image was 30.36 s (1.2 scanning cycle × 512 scanning points × 512 repeated times /10,360 sampling frequency). Thus, the acquisition time spending on vibrational OCE system for each hydrogel should be 30.42 s. The total time for each hydrogel was examined within 3 mins to minimise cell death during acquisition.

2.5.1. Maximum thickness measurement

The maximum thickness of dome shape hydrogels was non-destructively measured from the maximum cross-sectional image acquired by OCT system in a 15-day culture period, with pixels from peak to bottom. An example of the maximum thickness of an unwounded no-cell control on day 1 was measured from the maximum cross-sectional image (Fig. 3). According to the length of each pixel, the maximum thickness of the unwounded models is calculated as

$$H_h = P_h \times H_p \tag{1}$$

where H_h is the maximum thickness of the unwounded hydrogels, P_h is the pixels from peak to bottom, H_P is the length of each pixel, i.e. 3.8 μm/pixel.

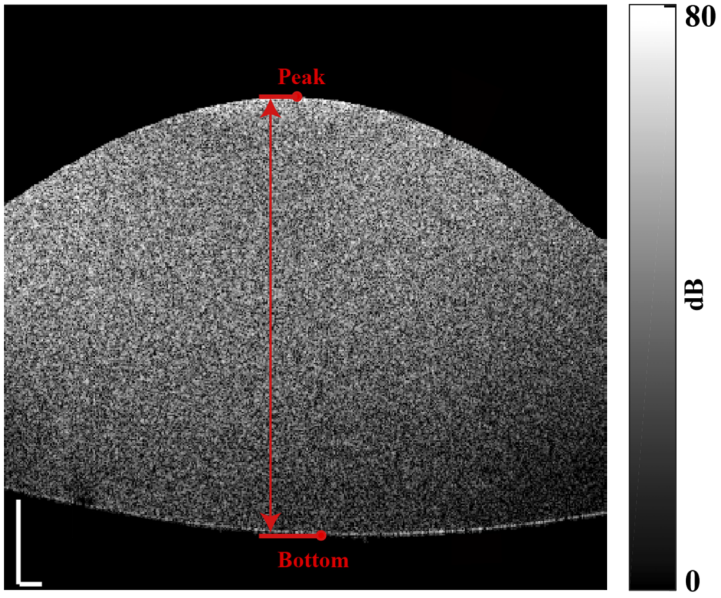

Fig. 3. An example of the maximum thickness measurement of an unwounded no-cell control on day 1. Measurement is pixels from peak to bottom in the maximum cross-sectional image in dB scale. The scale bar is 200 μm.

2.5.2. Elastography and analysis

A mathematic model was described by our group in previous study [41]. In our OCE system, the phase difference between the first and all the other A-lines at each depth is acquired. After

Biomedical Optics EXPRESS

applying FFT on the phase difference for each point on the A-line, the phase FFT amplitude signal as function of depth can be obtained. The phase FFT amplitude of sample is fitted by a linear polynomial model, after this, the slope of the linear fit can be calculated. The local strain is decided by the displacement of the sample, which is induced by the vibration amplitude, hence the vibration amplitude is directly related to the strain. As the phase FFT amplitude has linear relation to the correlation with vibration amplitude, the ratio of the slopes of phase FFT amplitude between sample and reference layer represents the ratio of strain. In the application of OCE, uniform stress fields are assumed to exert on each layer, thus, the ratio of strain is inversely proportional to ratio of elastic modulus. The elastic modulus of the hydrogels is calculated by the ratio of slopes of phase FFT amplitude between hydrogel and reference silicone, denoted as

$$E_h = \frac{S_s}{S_h} \times E_s \tag{2}$$

Where E_h is the elastic modulus of the hydrogels, E_s is the elastic modulus of the silicone, S_s and S_h are slope of phase FFT amplitude from silicone and hydrogels respectively.

In order to precisely and reliably measure the elastic modulus of the unwounded models from equation [Eq. (2)], the mean value of ratio of slopes of phase FFT amplitudes curves between unwounded models and silicone was measured with 70 frame numbers (1.17 mm – 2.34 mm) in the central area, where had a stable vibration than the two edges of the unwounded models.

To analyse the elastic modulus of the wounded constructs during wound healing by the dual-arm OCE setup, the measurement method is the same to above, by detecting the ratio of the slopes of phase FFT amplitude curves from neo-tissue in wound area and surrounding normal tissue. As the surrounding normal tissue is assumed to have equivalent elastic modulus to the unwounded constructs measured from equation [Eq. (2)] at the same time points, the elastic modulus of the neo-tissue in the wound area can be obtained by

$$E_w = \frac{S_h}{S_w} \times E_h \tag{3}$$

Where E_W is the elastic modulus of the neo-tissue, E_h is the elastic modulus of the unwounded hydrogels, S_w and S_h are slopes of phase FFT amplitude curves from neo-tissue and surrounding normal tissue in the wounded constructs, respectively.

3. Results

3.1. Cell morphology in unwounded construct

By the microscopic observation, the morphology of keratocytes in the unwounded constructs was obtained on day 3, day 7, day 13 and day 15, with 40×, 100× and 200× magnification times (Fig. 4). Keratocytes were shown to have proliferated rapidly within 13 days in culture, then showed less change in cell population between day 13 and day 15.

3.2. Unwounded corneal stroma model

3.2.1. Vibrational OCE results

To quantitatively calibrate the elastic modulus of the unwounded models, the structure images and elastograms were acquired by the vibrational OCE system during a 15-day culture period. Figure 5 shows the structure images and elastograms of the unwounded models on day 3, day 7 and day 13. As the unwounded models were much softer than the silicone, the colour bar of the elastograms was rendered as 1/Strain in dB scale to better visualise the change in stiffness of the unwounded models by comparing to the silicone. Under the assumption of uniform stress fields, strain is inversely proportional to elastic modulus. Thus, a greater value in the elastograms represented a stiffer property. The structure images of the unwounded controls (Fig. 5 (1a to 1c))

Biomedical Optics EXPRESS

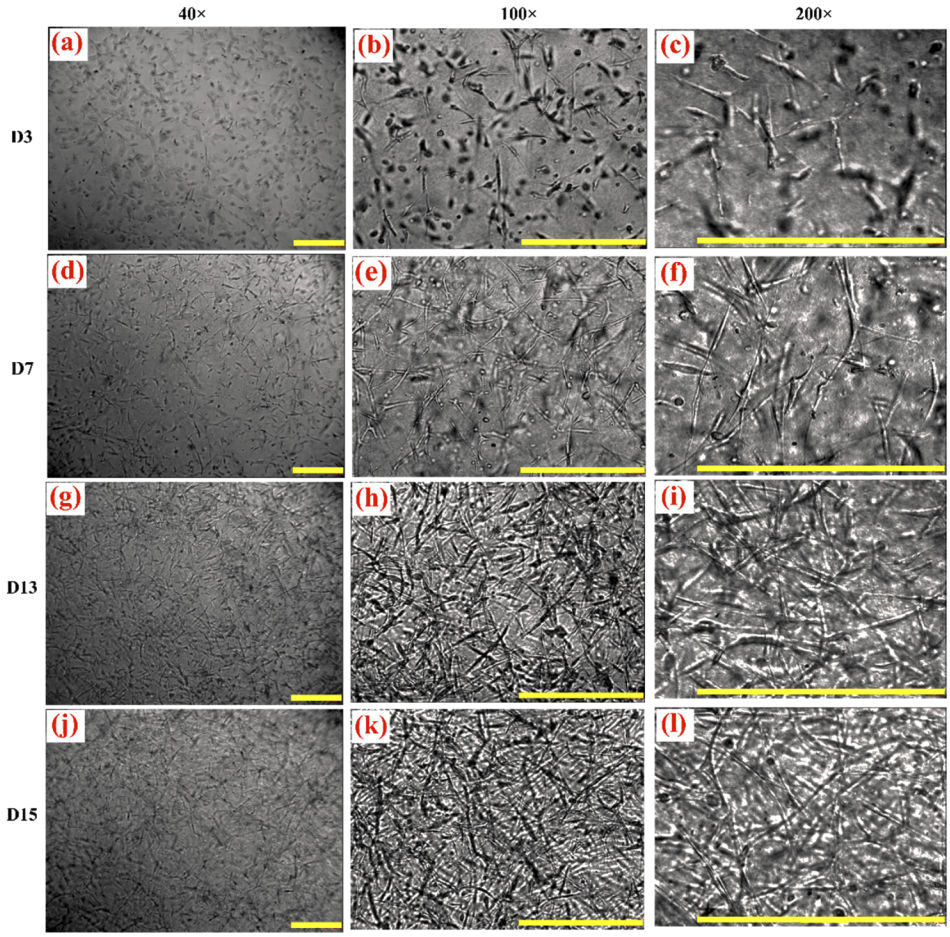

Fig. 4. The morphology of keratocytes in the unwounded constructs with light microscope imaging on day 3(a-c), day 7(d-f), day 13(g-i), day 15(j-l). The magnification times of the images from left to right are 40×, 100× and 200×. The scale bar is 500 μm.

showed less change in the thickness on day 3, day 7 and day 13. The value of the controls in the corresponding elastograms (Fig. 5 (1d to 1f)) showed similar value of 1/Strain in dB, with about 46 dB at three different time points. The thickness of the constructs became thinner as displayed in the structure images (Fig. 5 (2a to 2c)) on day 3, day 7 and day 13. The elastograms (Fig. 5 2d to 2f) demonstrated that the value of the constructs was approximate 47 dB, 49 dB and 54 dB on day 3, day 7 and day 13. The same silicone was used to calibrate the elastic modulus of the controls and the constructs, with the value of 71 dB in the elastograms.

The elastic modulus of the unwounded constructs (Fig. 6 (a)) experienced a slight increase, from 2.950 ± 0.2 kPa on day 1 to 3.250 ± 0.08 kPa on day 7. In the following 8 days, the elastic modulus of the constructs was raised remarkably by 7.910 kPa, with 11.0 ± 1.4 kPa on day 15 in culture. By contrast, the elastic modulus of the controls was 3.170 ± 0.1 kPa on day 1 and displayed a constant elastic modulus with around 3 kPa in 15 days.

3.2.2. Maximum thickness measurement

The maximum thickness of the unwounded models was measured from OCT structure images (Fig. 6 (b)). The maximum thickness of the controls had small fluctuations with the mean value

Biomedical Optics EXPRESS

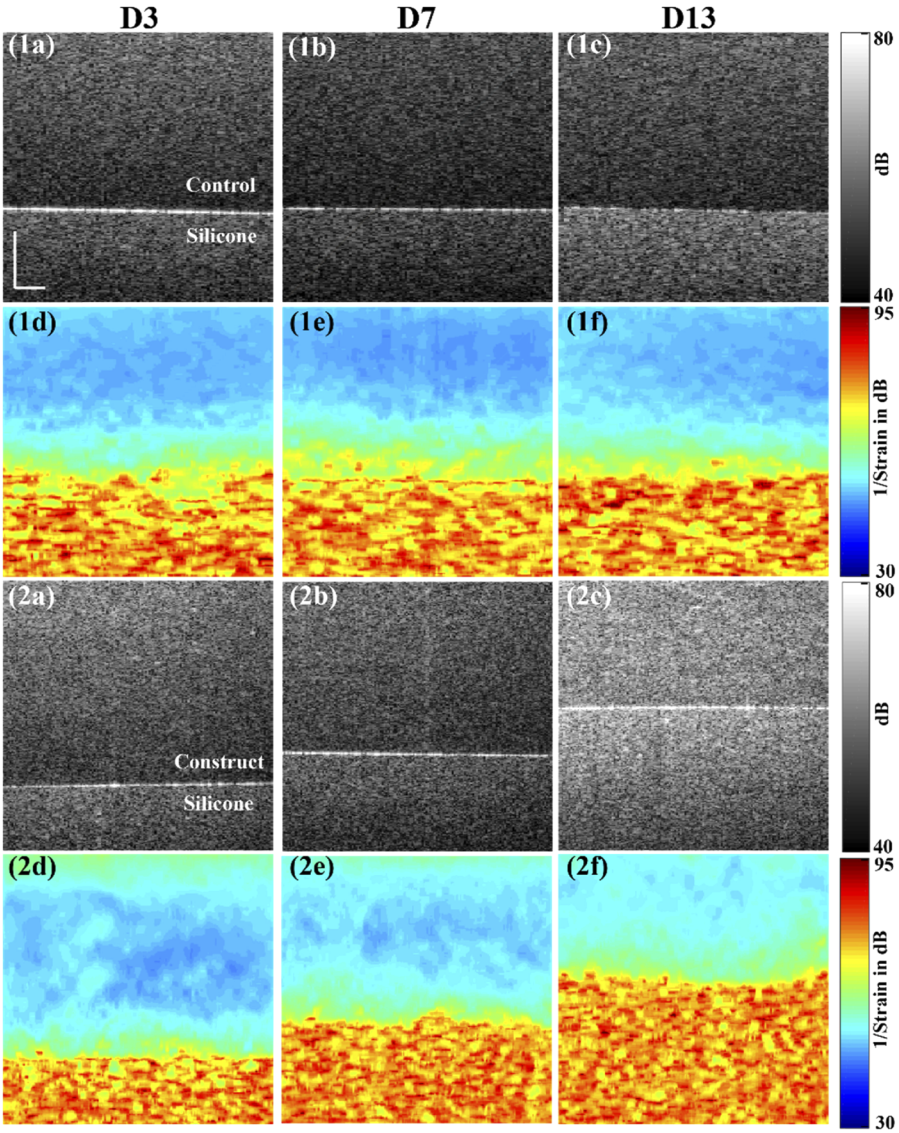

Fig. 5. Structure images in dB scale (a,b,c) and corresponding elastograms (d,e,f) of the unwounded controls (1) and the constructs (2) with a silicone underneath on day 3, day 7, day 13 acquired by vibrational OCE system. The colour bar in elastograms shows the value in unit of 1/Strain in dB scale. The scale bar is 200 μm.

Biomedical Optics EXPRESS

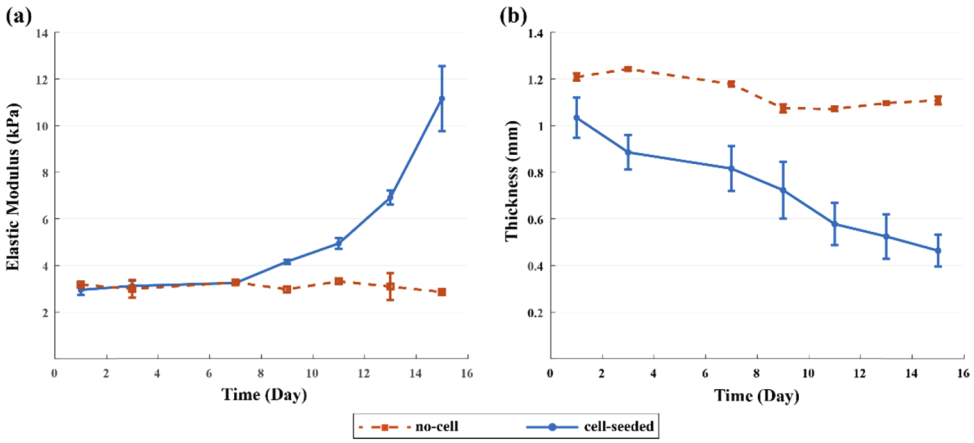

Fig. 6. Elastic modulus (a) and maximum thickness (b) of unwounded cell-seeded constructs (blue line) and no-cell controls (red line) in 15 days.

of 1.208 mm before day 7 and 1.096 mm after day 9. Between day 7 and day 9, a 0.1 mm decrease in the maximum thickness was observed. By contrast, the maximum thickness of the constructs became significantly thinner (P=0.0017), which dropped from 1.034 ± 0.1 mm on day 1 to 0.464 ± 0.09 mm on day 15.

3.3. *Vibrational OCE results of wounded corneal stroma model*

The change in stiffness of wound healing in the wounded constructs were monitored by the vibrational OCE system, with structure images and elastograms acquired (Fig. 7). The neo-tissue regenerated in wound area from day 3 and gradually closed the wound within 13 days shown from the structure images (Fig. 7 (1a to 4a)). In the corresponding elastograms (Fig. 7 (1b to 4b)), the colour bar represented the value of elastic modulus from 0 kPa to 16 kPa and stiffer area was represented as a darker colour in the elastograms. From the method described, the

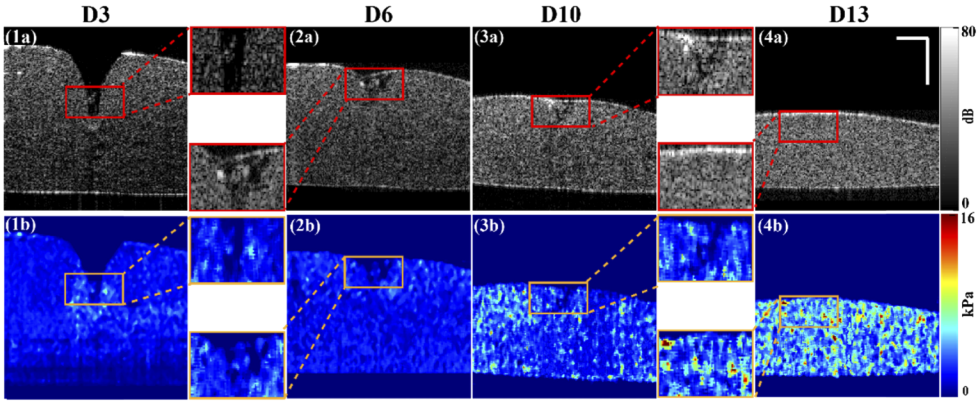

Fig. 7. Structure images in dB scale (1a, 2a, 3a, 4a) and corresponding elastograms (1b, 2b, 3b, 4b) of the wounded constructs on day 3, day 6, day 10 and day 13. The neo-tissue in wound area of the constructs in structure images and elastograms are marked and enlarged with red and orange rectangle respectively on day 3, day 6, day 10 and day 13. The colour bar in elastogram shows the value in unit of kPa. Label rectangle with size of 1.3 mm × 0.13 mm. The lateral scale bar is 1 mm. The axial scale bar is 200 μm.

Biomedical Optics EXPRESS

quantitative elastic modulus of the neo-tissue in the constructs obtained through comparing to the surrounding normal tissue on day 3, day 6, day 10 and day 13 were 1.488 ± 0.4 kPa, 1.749 ± 0.1 kPa, 3.422 ± 0.4 kPa and 6.639 ± 0.3 kPa respectively. The difference in elastic modulus between neo-tissue and surrounding normal tissue was gradually narrow, from 1.635 kPa on day 3 dropping to 0.282 kPa on day 13 (Fig. 8).

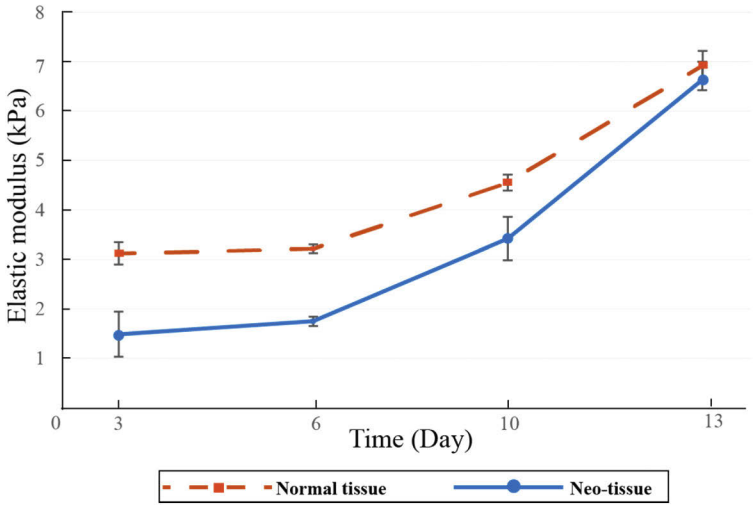

Fig. 8. Elastic modulus of the neo-tissue (blue line) and the surrounding normal tissue (orange line) in the wounded constructs during wound healing on day 3, day 6, day 10 and day 13 in culture.

4. Discussion

In this study, 3D wounded corneal stroma models were reconstructed using tissue-engineered approach, and the mechanical properties involving the maximum thickness and the elastic modulus of the models were monitored by a vibrational OCE system in continuous culture periods. Importantly, the change in elastic modulus of wound healing in the models was non-destructively monitored.

Corneal wound healing is an extremely complicated process, including the simultaneous multiple biochemical signals to regulate activities of cells alongside the chemical and biophysical characters of cellular matrix in the wound area [3,7]. Stroma has main injury response on mechanics [10]. In the initial wound response, a part of keratocytes turn into activated with appearance like fibroblast, and these cells migrate to the injury area within hours. Then, keratocytes experience apoptosis sequentially activating neighbouring keratocytes to achieve wound healing regulation. Finally, myofibroblasts migrate into the wound area and begin to remodel the stroma as its property of contraction [2,42]. But the stiffness variation caused by cell behaviours during wound healing is not fully understood.

Besides, in the stroma, collagen type I plays a role as the main mechanical and structural protein in the ECM. Thus, collagen hydrogel with keratocyte seeded is suitable for remodelling the corneal stoma *in-vitro* [15,16]. Our corneal stroma wound model has a distinct capacity in monitoring of wound healing processes and drug effects [43].

In practical examination of the unwounded models, three repeats of the constructs and the controls were conducted. To observe the change in stiffness of the wounded healing processes, five repeats of the wounded constructs were used to ensure the reproductivity. The constructs were successfully fabricated, indicated by keratocytes survival and continuous proliferation with

Biomedical Optics EXPRESS

microscopic observation. By using the common-path OCE setup, the unwounded constructs exhibited the decreased thickness and the stiffer property in a 15-day culture period, probably due to keratocytes mechanical interaction with surrounding extracellular matrix [44], proliferation, attachment throughout the hydrogel [45] and contraction of the hydrogel [46]. Moreover, the wounded constructs were non-destructively monitored with the dual-arm OCE setup in 13 days. Through observation the elastograms of the wounded models in Fig. 7, the tissue in wound edges had higher stiffness on day 3, probably due to quiescent keratocytes activated to fibroblasts. These fibroblasts migrated to close the wound [42] and participated in the remodelling phase, such as increasing expression of matrix metalloproteases (MMP). From day 3 to day 10, the increase of stiffness was possibly because the matrix changed to a collagen and proteoglycan matrix to increase the tissue strength. Growth factors accelerated the formation and cross-linking of the collagen fibre to increase stiffness and mechanical load [47]. On day 13, there was no distinct difference between neo-tissue and surrounding normal tissue in the wounded constructs.

As the features of non-invasive imaging and ultra-high resolution, OCT has been widely used in observation of corneal wound healing. The microstructural alterations during the healing process can be detailed assessed. Compared to traditional clinical evaluation such as corneal fluorescein staining and slit lamp testing, OCT provides higher accuracy, and 3D mapping of the wound in the cornea. Lal et al. [31] described a nano-scale OCT (nsOCT) system to analyse micro-structural changes within a rat cornea by acquiring the spatial period parameter. Nanoscale structural changes of wound healing in the rat cornea were accessed on day 1 and day 7 after alkali injury. The results suggested the increased spatial period of the alkali injured cornea when comparing with the healthy cornea. The nsOCT provides potential for *in-vivo* imaging in clinical application to detect the abnormal structure or observe the wound healing processes in nano-scale. Also, the nsOCT has nano-scale resolution vs. our micro-scale resolution and has fast processing time based on single frame vs. our MB-scan protocol. However, the quantitative mechanical information cannot be obtained from the value of spatial period. As known, quantitative mechanical properties of tissue are important in assessment of pathological and physiological processes. Hepburn et al. [48] used a 3D quantitative micro-elastography (QME) to measure the elasticity of EMC in the gelatine hydrogels. The results shown the TAZ (a mechanosensitive transcription factor) activation in human adipose-derived stem cells (ASCs) resulted in an increasing elasticity of the cells and the ECM in the hydrogels. 3D imaging offers volumetric structure image and distribution of elasticity over time in 3D biomaterial. Our method has strong potential to realise 3D OCT and OCE imaging of wound healing in the corneal stroma wound model by acquiring consecutive B-scans. Moreover, in the QME, the elasticity of cell size larger than 39 μm can be imaged and the imaging depth of sample is 0.45 mm. By comparison, our vibrational OCE system cannot reach such a small resolution in the elastogram but the imaging depth is about 2 mm, which is more flexible in most application of biomaterials, especially corneal model. The main restriction in application of the QME is a compression force need to be applied to the sample through an imaging window, which will contaminate the sample. Hence, the QME is difficult to continuously monitor the mechanical changes in sample. In our setup, the dual-arm OCE as a non-contact method can be applied to monitor the stiffness change in the sample over a continuous culture period.

To our knowledge, few papers [49–54] have investigated OCE technique in detecting biomechanical properties of tissue-engineered materials, but there is less investigation relative to OCE methods detecting biomechanics during the wound healing processes.

Ko et al. [49] firstly combined tissue-engineered material with OCE system. In this paper, a reconstructed sample consisted of two components, the left section seeded with cells and no cell in the other side. A glass slide compressed on sample and static compression was applied on it. It could be seen a smaller displacement and strain in the cell-seeded section than control section, as cell behaviours and ECM changes resulted in tissue getting stiffer. The shortcoming

Biomedical Optics EXPRESS

for static compression OCE is obvious. For instance, it requires contact with sample, which cannot realise non-destructively detect the wound healing process in sample. Guan et al. [50] applied vibrational OCE to detect elasticity of bone tissue constructs. In this approach, agar solution was poured into the constructs to qualitatively obtain the stiffness from elastograms. Nevertheless, this approach also could not continuously monitor the changes in constructs and was destructive to the sample.

In addition, the biomechanics of corneal stroma bulky hydrogel has been well studied. Ahearne et al. [51] reported a spherical indentation technique to reveal biomechanical relationship between cell and matrix in hydrogels over 25 days. The results indicated lower initial collagen concentration and larger numbers of cell seeded in the hydrogels had weaker resistance for contraction. Moreover, the thickness of no-cell hydrogel was around 1.1 mm, similar with our findings. The elastic modulus of hydrogel with collagen concentration of 2.5 mg/mL and cell density of 5×10^5 cells/mL also had a similar rise trend with our unwounded hydrogel, and finally reached to about 11 kPa on day 25. Law et al. [52] used the same technique to investigated collagen hydrogels with fibroblasts, keratinocytes and nanofibers in 22 days. The study showed a similar increase in the trend of elastic modulus with us, but the final value was about 7.8 kPa. Their interpretation was that a decreased cell number induced lower force of contraction, leading to a lower elastic modulus of hydrogel. Although the spherical indentation technique is non-destructive and quantitative monitoring the stiffness of bulky sample, the localized elasticity distribution of the sample and epically healing processes of defect in the sample could not be quantified.

Leartprapun et al. [53] developed a photonic force OCE (PF-OCE) to track the radiation pressure induced oscillation of 3-μm and 0.1-μm beads in viscoelastic hydrogels. The results indicated that the mechanical parameters of the hydrogels varied with agarose concentrations. Besides, with the increase of the agarose concentrations, the hydrogels became more elastic. According to this method, the sensitivity of oscillation amplitude detection can reach ~105 pm and volumetric imaging of bead responses in hydrogels can be measured. The imaging depth of the PF-OCE depends on mechanical response of PF beam focal plane, with 200 μm. However, this shallow imaging depth restricts the practical uses of the PF-OCE, such as corneal model or others tissue-mimicking biomaterials. In our study, although the minimum displacement can be detected as 2 nm in sample, it is enough to detect the displacement of sample within 1 μm. Excepting elastic modulus, viscous parameters in viscoelastic measurement of tissue can provide useful information in diagnosis. Zvietcovich et al. [54] proposed an inversion of wave propagation model in OCE system. The acoustic radiation force (ARF) excitation on collagen hydrogels was produced to estimate the viscoelasticity. The results indicated that with the increasing collagen concentrations from range of 2 mg/mL to 6.7 mg/mL in the hydrogels, shear speed parameter gradually decreased, and attenuation coefficient showed an increasing tendency. Thus, higher collagen concentration may result in higher viscous property, in turn to influence elasticity of hydrogel. In our study, although we used the hydrogels with a relative low collagen concentration (3 mg/mL) and a low vibration frequency of 225 Hz to avoid obvious viscous effect [40], the viscous property indeed can affect the biomechanical properties, thereby impacts the wound healing processes. In further research, we will discuss the viscoelastic property in the corneal stroma model. In addition, ultra-fast wave-based OCE techniques [33–35] have been developed to largely reduce the acquisition time to millisecond scale. However, the vibrational OCE has much higher lateral resolution, which suits better for monitoring the wound healing processes in the corneal wound model. Meanwhile, phase FFT amplitude algorithm can eliminate noise and other co-generated vibrational modes, leading to a high SNR [37].

Besides the advantages of our vibrational OCE system in quantitative monitoring mechanical changes in the corneal stroma wound models, this study also has limitations. Although wound healing processes in the wounded constructs were non-destructively monitored by the dual-arm

Biomedical Optics EXPRESS

OCE setup over a continuous culture period, the stiffness of the unwounded models was calibrated via vibrating together with a reference silicone layer in the common-path OCE setup. Also, the real human cornea is consisted of epithelium, stroma, and endothelium layers. There are interactions between layers, such as stromal-epithelial [55] and stromal-endothelial interactions [56] during healing processes. Our current corneal stroma wound model just mimics the stromal layer of the cornea, which can not reveal the interactions between corneal layers. In addition, we avoided the evident viscoelastic property of the collagen hydrogel with a low excitation frequency, but viscoelasticity indeed exists, and cells can sense viscoelasticity of ECM [57]. Finally, previous study [58] reported corneal stroma neovascularisation frequently happens in severe corneal trauma, due to inflammation, gene mutations and decreased generation of anti-angiogenic molecules [59]. But the neovascularisation is not repressed in the current corneal stroma wound model. Therefore, in the future, the above limitations will be overcome.

5. Conclusion

In conclusion, we innovatively demonstrate a vibrational OCE method, which is capable of monitoring the quantitative changes in biomechanical properties of a 3D corneal stroma wound model during wound healing over a continuous culture period.

Funding

National Centre for the Replacement Refinement and Reduction of Animals in Research (10945a_CRT).

Disclosures

The authors declare no conflicts of interest.

See Supplement 1 for supporting content.

References

1. M. F. Land and R. D. Fernald, "The evolution of eyes," Annu. Rev. Neurosci. **15**(1), 1–29 (1992).
2. D. W. DelMonte and T. Kim, "Anatomy and physiology of the cornea," J. Cataract Refractive Surg. **37**(3), 588–598 (2011).
3. A. V. Ljubimov and M. Saghizadeh, "Progress in corneal wound healing," Prog. Retinal Eye Res. **49**, 17–45 (2015).
4. M. A. Stepp, J. D. Zieske, V. Trinkaus-Randall, B. M. Kyne, S. Pal-Ghosh, G. Tadvalkar, and A. Pajoohesh-Ganji, "Wounding the cornea to learn how it heals," Exp. Eye Res. **121**, 178–193 (2014).
5. J. Wipperman and J. N. Dorsch, "Evaluation and management of corneal abrasions," American Family Physician **87**(2), 114–120 (2013).
6. S. F. Wilson and A. R. Last, "Management of corneal abrasions," American Family Physician **70**(1), 123–128 (2004).
7. S. E. Wilson, R. R. Mohan, R. R. Mohan, R. A. Jr, J. Hong, and J. Lee, "The corneal wound healing response: cytokine-mediated interaction of the epithelium, stroma, and inflammatory cells," Prog. Retinal Eye Res. **20**(5), 625–637 (2001).
8. S. Saika, "TGFbeta pathobiology in the eye," Lab. Invest. **86**(2), 106–115 (2006).
9. A. Tandon, J. C. K. Tovey, A. Sharma, R. Gupta, and R. R. Mohan, "Role of transforming growth factor beta in corneal function, biology and pathology," Curr. Mol. Med **10**(6), 565–578 (2012).
10. W. J. Dupps and S. E. Wilson, "Biomechanics and wound healing in the cornea," Exp. Eye Res. **83**(4), 709–720 (2006).
11. Y. Zhao, Y. Yang, R. K. Wang, and S. A. Boppart, "Optical coherence tomography in tissue engineering," in *Optical Coherence Tomography* (Springer, 2015), pp. 889–917.
12. M. R. Prausnitz and J. S. Noonan, "Permeability of cornea, sciera, and conjunctiva: A literature analysis for drug delivery to the eye," J. Pharm. Sci. **87**(12), 1479–1488 (1998).
13. K. Bardsley, A. J. Deegan, A. El Haj, and Y. Yang, "Current state-of-the-art 3D tissue models and their compatibility with live cell imaging," Adv. Exp. Med. Biol **1035**, 3–18 (2017).
14. M. C. Cushing and K. S. Anseth, "Hydrogel cell cultures," Science **316**(5828), 1133–1134 (2007).

Biomedical Optics EXPRESS

15. A. Kim, N. Lakshman, D. Karamichos, and W. Matthew Petroll, "Growth factor regulation of corneal keratocyte differentiation and migration in compressed collagen matrices," Invest. Ophthalmol. Visual Sci. **51**(2), 864–875 (2010).
16. X. Duan, C. McLaughlin, M. Griffith, and H. Sheardown, "Biofunctionalization of collagen for improved biological response: Scaffolds for corneal tissue engineering," Biomaterials **28**(1), 78–88 (2007).
17. S. L. Wilson, M. Ahearne, A. J. El Haj, and Y. Yang, "Mechanical characterization of hydrogels and its implications for cellular activities," RSC Soft Matter **2014**, 171–190 (2014).
18. M. Ahearne and D. J. Kelly, "A comparison of fibrin, agarose and gellan gum hydrogels as carriers of stem cells and growth factor delivery microspheres for cartilage regeneration," Biomed. Mater. **8**(3), 035004 (2013).
19. M. Ahearne, P. O. Bagnaninchi, Y. Yang, and A. J. El Haj, "Online monitoring of collagen fibre alignment in tissue-engineered tendon by PSOCT," J. Tissue Eng. Regener. Med. **2**(8), 521–524 (2008).
20. A. F. Fercher, W. Drexler, C. K. Hitzenberger, and T. Lasser, "Optical coherence tomography - Principles and applications," Rep. Prog. Phys **66**(2), 239 (2003).
21. M. R. Hee, J. A. Izatt, E. A. Swanson, D. Huang, J. S. Schuman, C. P. Lin, C. A. Puliafito, and J. G. Fujimoto, "Optical coherence tomography of the human retina," Arch. Ophthalmol. **113**(3), 325–332 (1995).
22. M. E. J. van Velthoven, D. J. Faber, F. D. Verbraak, T. G. van Leeuwen, and M. D. de Smet, "Recent developments in optical coherence tomography for imaging the retina," Prog. Retinal Eye Res. **26**(1), 57–77 (2007).
23. N. D. Gladkova, N. D. Gladkova, G. A. Petrova, N. K. Nikulin, S. G. Radenska-Lopovok, L. B. Snopova, Y. P. Chumakov, V. A. Nasonova, V. M. Gelikonov, G. V. Gelikonov, R. V. Kuranov, A. M. Sergeev, and F. I. Feldchtein, "In vivo optical coherence tomography imaging of human skin: Norm and pathology," Ski. Res. Technol **6**(1), 6–16 (2000).
24. W. Drexler, D. Stamper, C. Jesser, X. Li, C. Pitris, K. Saunders, S. Martin, M. B. Lodge, J. G. Fujimoto, and M.E. Brezinski, "Correlation of collagen organization with polarization sensitive imaging of in vitro cartilage: Implications for osteoarthritis," J. Rheumatol **28**(6), 1311–1318 (2001).
25. M. Eliaçik, H. Bayramlar, S. K. Erdur, Y. Karabela, G. Demirci, İG Gülkilik, and M. Özsütçü, "Anterior segment optical coherence tomography evaluation of corneal epithelium healing time after 2 different surface ablation methods," Saudi Med. J. **36**(1), 67–72 (2015).
26. K. Zheng, H. Huang, K. Peng, J. Cai, V. Jhanji, and H. Chen, "Change of optical intensity during healing process of corneal wound on anterior segment optical coherence tomography," Sci. Rep. **6**(1), 32352 (2016).
27. T. Utsunomiya, K. Hanada, O. Muramatsu, A. Ishibazawa, N. Nishikawa, and A. Yoshida, "Wound healing process after corneal stromal thinning observed with anterior segment optical coherence tomography," Cornea **33**(10), 1056–1060 (2014).
28. C. E. Pang, M. Vanathi, D. T. Tan, and J. S. Mehta, "Evaluation of corneal epithelial healing under contact lens with spectral-domain anterior segment optical coherence tomography (SDOCT)," Open Ophthalmol. J. **5**(1), 51–54 (2011).
29. A. Pantalon, M. Pfister, V. Aranha dos Santos, S. Sapeta, A. Unterhuber, N. Pircher, G. Schmidinger, G. Garhöfer, D. Schmidl, L. Schmetterer, and R. M. Werkmeister, "Ultrahigh-resolution anterior segment optical coherence tomography for analysis of corneal microarchitecture during wound healing," Acta Ophthalmol. **97**(5), e761–e771 (2019).
30. V. K. Raghunathan, S. M. Thomasy, P. Strøm, B. Yañez-Soto, S. P. Garland, J. Sermeno, C. M. Reilly, and C. J. Murphy, "Tissue and cellular biomechanics during corneal wound injury and repair," Acta Biomater. **58**, 291–301 (2017).
31. C. Lal, S. Alexandrov, S. Rani, Y. Zhou, T. Ritter, and M. M. Leahy, "Nanosensitive optical coherence tomography to assess wound healing within the cornea," Biomed. Opt. Express **11**(7), 3407–3422 (2020).
32. B. F. Kennedy, T. R. Hillman, R. A. McLaughlin, B. C. Quirk, and D. D. Sampson, "In vivo dynamic optical coherence elastography using a ring actuator," Opt. Express **17**(24), 21762–21772 (2009).
33. M. Singh, C. Wu, C. H. Liu, J. Li, A. Schill, A. Nair, and K. V. Larin, "Phase-sensitive optical coherence elastography at 1.5 million A-Lines per second," Opt. Lett. **40**(11), 2588–2591 (2015).
34. C. Wu, Z. Han, M. Singh, C. H. Liu, J. Li, A. Schill, R. Raghunathan, and K. V. Larin, "Magnetic force Optical Coherence Elastography at 1.5 million a-lines per second," Int. Soc. Opt. Eng. **9697**, 969734 (2016).
35. S. Song, B. Y. Hsieh, W. Wei, T. Shen, I. Pelivanov, M. O'nnell, and R. K. Wang, "Optical coherence elastography based on high speed imaging of single-hot laser-induced acoustic waves at 16 kHz frame rate," Int. Soc. Opt. Eng. **9697**, 96971O (2016).
36. F. Zvietcovich, J. P. Rolland, J. Yao, P. Meemon, and K. J. Parker, "Comparative study of shear wave-based elastography techniques in optical coherence tomography," J. Biomed. Opt **22**(3), 035010 (2017).
37. R. K. Wang and L. An, "Doppler optical micro-angiography for volumetric imaging of vascular perfusion in vivo," Opt. Express **17**(11), 8926–8940 (2009).
38. R. K. Wang, S. Kirkpatrick, and M. Hinds, "Phase-sensitive optical coherence elastography for mapping tissue microstrains in real time," Appl. Phys. Lett. **90**(16), 164105 (2007).
39. M. Ahearne, Y. Yang, K. Y. Then, and K. K. Liu, "Non-destructive mechanical characterisation of UVA/riboflavin crosslinked collagen hydrogels," Br. J. Ophthalmol. **92**(2), 268–271 (2008).
40. D. Zhang, J. Wang, C. Li, and Z. Huang, "Optimal stimulation frequency for vibrational optical coherence elastography," J. Biophotonics **13**(2), e201960066 (2020).

Biomedical Optics EXPRESS

41. G. Guan, C. Li, Y. Ling, Y. Yang, J. B. Vorstius, R. P. Keatch, R. K. Wang, and Z. Huang, "Quantitative evaluation of degenerated tendon model using combined optical coherence elastography and acoustic radiation force method," J. Biomed. Opt **18**(11), 111417 (2013).
42. J. A. West-Mays and D. J. Dwivedi, "The keratocyte: Corneal stromal cell with variable repair phenotypes," Int. J. Biochem. Cell Biol. **38**(10), 1625–1631 (2006).
43. C. Fischak, R. Klaus, R. M. Werkmeister, C. Hohenadl, M. Prinz, L. Schmetterer, and G. Garhöfer, "Effect of topically administered chitosan-N-acetylcysteine on corneal wound healing in a rabbit model," J. Ophthalmol. **2017**, 5192924 (2017).
44. W. M. Petroll and M. Miron-Mendoza, "Mechanical interactions and crosstalk between corneal keratocytes and the extracellular matrix," Exp. Eye Res. **133**, 49–57 (2015).
45. K. Takakuda and H. Miyairi, "Tensile behaviour of fibroblasts cultured in collagen gel," Biomaterials **17**(14), 1393–1397 (1996).
46. E. Bell, B. Ivarsson, and C. Merrill, "Production of a tissue-like structure by contraction of collagen lattices by human fibroblasts of different proliferative potential in vitro," Proc. Natl. Acad. Sci. **76**(3), 1274–1278 (1979).
47. W. Wu and Y. Wang, "The wound healing responses and corneal biomechanics after keratorefractive surgery," *Wound Healing-Current Perspectives* (IntechOpen, 2018).
48. M. S. Hepburn, P. Wijesinghe, L. G. Major, J. Li, A. Mowla, C. Astell, H. W. Park, Y. Hwang, Y. S. Choi, and B. F. Kennedy, "Three-dimensional imaging of cell and extracellular matrix elasticity using quantitative micro-elastography," Biomed. Opt. Express **11**(2), 867–884 (2020).
49. H. J. Ko, W. Tan, R. Stack, and S. A. Boppart, "Optical coherence elastography of engineered and developing tissue," Tissue Eng. **12**(1), 63–73 (2006).
50. G. Guan, S. Song, Z. Huang, and Y. Yang, "Application of new optical coherence elastography to monitor the mineralization processing in bone tissue engineering constructs," *Dynamics and Fluctuations in Biomedical Photonics XII*, 93220G (2015).
51. M. Ahearne, Y. Yang, A. J. El Haj, K. Y. Then, and K. K. Liu, "Characterizing the viscoelastic properties of thin hydrogel-based constructs for tissue engineering applications," J. R. Soc. Interface. **2**(5), 455–463 (2005).
52. J. X. Law, F. Musa, B. H. I. Ruszymah, A. J. El Haj, and Y. Yang, "A comparative study of skin cell activities in collagen and fibrin constructs," Med. Eng. Phys **38**(9), 854–861 (2016).
53. N. Leartprapun, R. R. Iyer, G. R. Untracht, J. A. Mulligan, and S. G. Adie, "Photonic force optical coherence elastography for three-dimensional mechanical microscopy," Nat. Commun. **9**(1), 2079 (2018).
54. F. Zvietcovich, J. P. Rolland, E. Grygotis, S. Wayson, M. Helguera, D. Dalecki, and K. J. Parker, "Viscoelastic characterization of dispersive media by inversion of a general wave propagation model in optical coherence elastography," J. Innov. Opt. Health Sci. **10**(06), 1742008 (2018).
55. C. M. Nieto, L. C. Rider, and S. D. Cramer, "Influence of stromal-epithelial interactions on androgen action," Endocr.-Relat. Cancer **21**(4), T147–T160 (2014).
56. C. S. Medeiros, L. Lassance, P. Saikia, M. Santhiago, and S. E. Wilson, "Posterior stromal cell apoptosis triggered by mechanical endothelial injury and basement membrane component nidogen-1 production in the cornea," Exp. Eye Res. **172**, 30–35 (2018).
57. S. Nam, K. H. Hu, M. J. Butte, and O. Chaudhuri, "Strain-enhanced stress relaxation impacts nonlinear elasticity in collagen gels," Proc. Natl. Acad. Sci. **113**(20), 5492–5497 (2016).
58. Z. Sharif and W. Sharif, "Corneal neovascularization: updates on pathophysiology, investigations & management," rjo **63**(1), 15–22 (2019).
59. P. Lim, T. A. Fuchsluger, and U. V. Jurkunas, "Limbal stem cell deficiency and corneal neovascularization," Semin. Ophthalmol. **24**(3), 139–148 (2009).